Numerical Simulation of Airfoil Thermal Anti-Ice Operation Part 2: Implementation and Results

Guilherme Araújo Lima da Silva,* Otávio de Mattos Silvares,† and
Euryale Jorge de Godoy Jesus Zerbini‡
Escola Politécnica, University of São Paulo, 05508-900 São Paulo, Brazil

DOI: 10.2514/1.24922

This paper presents the implementation and results of the airfoil electrothermal anti-ice mathematical model developed in part 1 (Silva, G. A. L, Silvares, O. M., Zerbini, E. J. G. J., "Numerical Simulation of Airfoil Thermal Anti-Ice Operation Part 1: Mathematical Modeling", *Journal of Aircraft*, submitted for publication). From flowfield and supercooled water droplet impingement data up to electrical power density distribution, the numerical code is able to predict airfoil solid surface temperature and runback water mass flow rate distributions around an airfoil provided with ice protection. The numerical predictions were compared with both experimental data and other numerical codes results for selected reference cases. The present code satisfactorily predicted the coupled convection heat and mass transfer effects between the nonisothermal surface and the gaseous flow around the airfoil, as well as the influence of the runback water flow on the anti-ice system thermal performance.

Nomenclature

C_f	=	local friction coefficient $\tau/(1/2 \cdot \rho_e \cdot u_e^2)$
C_p	=	pressure coefficient, $(p_e - p_\infty)/(1/2 \cdot \rho_\infty \cdot u_\infty^2)$
c	=	airfoil chord, m
h	=	convective heat transfer coefficient, $W/(m^2 \cdot K)$
k	=	thermal conductivity, $W/(m \cdot K)$
$\dot{m}_{imp}$	=	impinging mass flux, $kg/(s \cdot m^2)$
p	=	pressure, Pa
s	=	streamwise distance on airfoil solid surface, m
T	=	temperature, °C
U	=	overall heat transfer coefficient, $W/(m^2 \cdot K)$
u	=	boundary layer streamwise velocity, m/s
V	=	velocity, m/s
α	=	angle of attack
β	=	local collection efficiency
ρ	=	density, kg/m^3
σ	=	transition region standard deviation length, m

Subscripts

air	=	gaseous flow around airfoil
e	=	external edge of boundary layer
∞	=	nondisturbed freestream flow
m	=	transition region mean position
tot	=	total
tr	=	laminar to turbulent flow abrupt transition position
wall	=	airfoil solid surface

*Graduate Student, Mechanical Engineering Department, Escola Politécnica, Avenida Professor Mello Moraes, 223; also Thermal Analyst, Environmental Systems Engineering, Embraer, São José dos Campos, Brazil, Brigadeiro Faria Lima, 2170. AIAA Member.

†Associate Professor, Mechanical Engineering Department, Escola Politécnica, Avenida Professor Mello Moraes, 2231; also Dean, University Dean Office, Praça Mauá 1, Instituto Mauá de Tecnologia, São Caetano do Sul, Brazil.

‡Professor, Mechanical Engineering Department, Avenida Professor Mello Moraes, 2231.

I. Objective

THE main objective of the present paper is to implement the mathematical model and simulate the operation of an electrothermal anti-ice device designed for aeronautical use. The mathematical procedure for estimation of airfoil anti-ice system operational parameters is published in part 1 of this set of papers [1]. Complementing the set, this part 2 describes the numerical code architecture and its validation process applied to the case of a NACA 0012 airfoil equipped with electrical heaters operating under icing conditions.

II. Numerical Code Architecture

The development and implementation of an airfoil anti-ice system numerical simulation [1–5] comprised the following: 1) application of an available external solver to the flow around the airfoil and to droplets trajectories; 2) development of a new thermodynamic solver (main program); 3) development of momentum and thermal boundary layer evaluation routines adequate for flow over nonisothermal and smooth surfaces with evaporation; and 4) validation of numerical predictions with reliable experimental data as well as other numerical codes results. The external solver ONERA2D requires a two-dimensional airfoil profile, atmospheric information [liquid water content (LWC), median volumetric diameter (MVD), T_∞, p_∞], and flight condition (V_∞, α) to provide pressure, velocity, and local collection efficiency distributions around the airfoil to the present code. ONERA2D was validated at a broad range of conditions with experimental data and had its results extensively compared with other numerical codes [2,6,7], therefore, its results are considered acceptable not requiring further validation. As a matter of fact, any other external solver can be used to generate inputs to the present code.

In the present paper, only two ONERA2D modules are used herein to generate input data for anti-ice numerical simulation: 1) a flow solver module that solves the full potential flow around airfoil by finite elements [8,9] with a C-type mesh (Fig. 1a); and 2) a water droplet trajectories module that predicts the local collection efficiency distribution on the airfoil surface [6] as shown in Fig. 1b. The other two remaining modules of external solvers (heat transfer and ice growth) were not applicable to the present development because they are specific for ice accretion simulation.

The implementation of a new thermodynamic solver together with a boundary layers evaluation routine were required because the ice-protected airfoil has a heated, permeable, nonisothermal, relatively smooth, and variable wetness surface interfacing with the boundary layer flow. These surface boundary conditions do not allow the
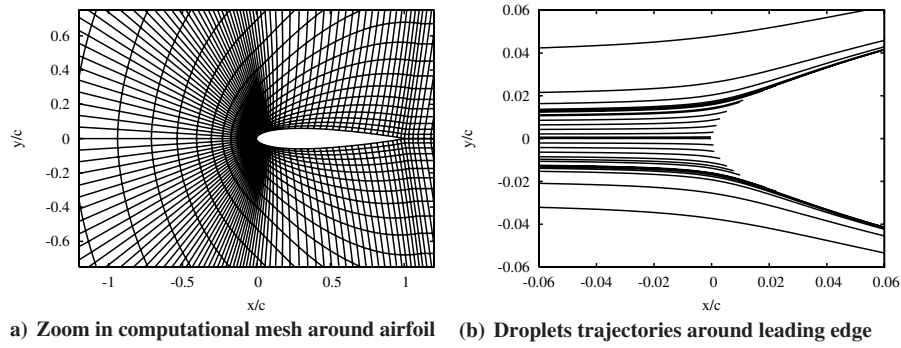
a) Zoom in computational mesh around airfoil (b) Droplets trajectories around leading edge

Fig. 1 External solver application on NACA0012 profile.

application of those mathematical models used in classic icing codes such as LEWICE , TRAJICE2 [12,13], or ONERA2D [6]. For instance, ONERA2D considers an abrupt transition from laminar to turbulent flow transition, estimates the convection heat transfer over rough quasi-isothermal icing surfaces , and applies Messinger's [15] thermal balance model to predict ice growth on unheated surfaces.

Therefore, to depict more real interfacing conditions required a new mathematical model which was developed by Silva et al. [1–5] for simulation of anti-ice systems. Its numerical implementation is summarized in Fig. 2. In sum, the thermodynamic solver collects data from the user and from the external flow solver and starts the calculation. A routine for momentum and thermal boundary layers evaluation provides h_{air} and C_f around the airfoil. Then the mass and momentum conservation equations are applied to liquid water film flow, and the first law of thermodynamics is applied separately to airfoil solid surface and liquid water film. The solution of the system of equations (T_{wall} and $\dot{m}_{run}$) in each finite volume is considered satisfactory when the convergence of heat and mass convection fluxes is verified. Thus, the equations are solved in all finite volumes at the lower surface from stagnation point to the airfoil trailing edge. Complimentarily, the same solution process is carried out also along the upper surface. The execution of the thermodynamic solver is repeated until the continuity of heat flux across the stagnation point is achieved. At the end of the solution process, the present code is able to estimate the anti-ice system operational parameters such as solid surface temperatures, runback water mass flow rate, and convection heat transfer coefficient distributions, as well as the end of water film positions at the airfoil solid surface.

III. Reference Cases

The reference cases choice was based on the existence of representative experimental data from a reliable source published in open literature. Al-Khalil et al. [16] performed anti-icing experiments at the Icing Research Tunnel at NASA Glenn Research Center facilities, Cleveland, Ohio, by measuring surface temperature and overall heat transfer coefficient to validate ANTICE numerical code results.

The airfoil tested [16] was a 1.828 m span by 0.914 m chord NACA 0012 profile (see Fig. 3) with electronically controlled heaters (A, B, C, D, E, F, and G) positioned as indicated in Table 1. Each heater element in the streamwise direction had one thermocouple, one thermoresistor sensor, and one heat flux gauge installed. There were two sets of electrical heaters placed side-by-side spanwise. Each heater set had seven individually controlled heater elements. The total protected area was 0.914 m spanwise (two heater sets of 0.457 m) by 0.197 m streamwise, both in upper and in lower surfaces.

Several cases were run in evaporative and running wet regimes by using an electrically heated airfoil to simulate an anti-ice system operation over a broad range of conditions. Three representative reference cases were chosen from a test data set to be simulated by the present code. Table 2 presents the cases and the respective test conditions. In addition, Table 1 lists the electrical power density distribution for each case and the position of the heater elements in streamwise coordinates.

In normal direction, from airfoil surface to gaseous flow, the heater element consists of silicone foam thermal insulation, fiber glass/ epoxy composite, an elastomer layer, heater resistance, another elastomer layer, and an external erosion shield. Table 3 presents the thermal conductivity and thickness of the materials used in heaters elements construction. The two-dimensional heat conduction in airfoil surface is approximated by a one-dimensional streamwise heat conduction problem. By considering the thermal resistance of the materials associated in parallel, from the heater to the external surface on the top (Table 3), and all layers at same average temperature, the estimated conductivity in streamwise direction is $k_{wall} = 4.7 \text{ W}/(\text{m}^2 \cdot \text{K})$.
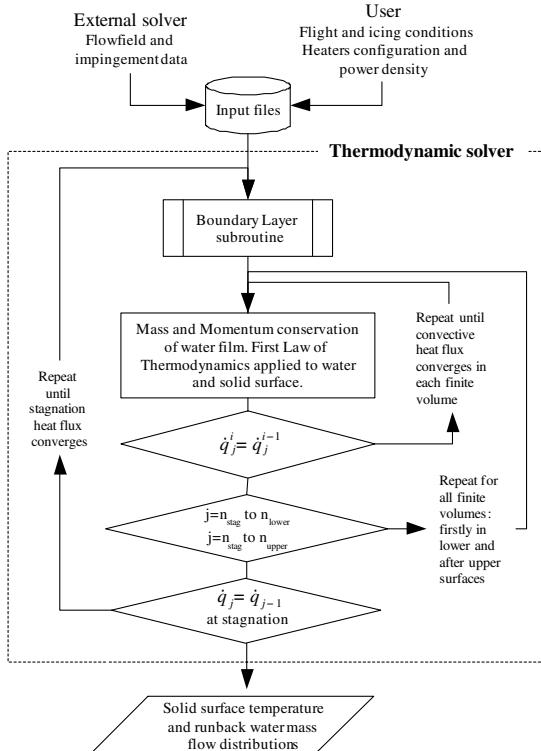

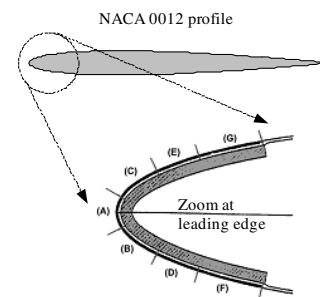Fig. 2 Brief description of numerical implementation.

Fig. 3 Heaters on NACA 0012 leading edge [16].

Table 1 Electric heaters lengths and power densities [16]

Heater element	Streamwise distance per chord		Anti-ice heat flux, kW · m⁻²		
	start	end	case 22A	case 67A	case 67B
F	−0.1024	−0.0607	9.92	20.15	8.37
D	−0.0607	−0.0329	10.23	21.7	11.94
B	−0.0329	−0.0051	32.5	32.55	10.85
A	−0.0051	0.0157	46.5	43.4	15.19
C	0.0157	0.0435	18.6	26.35	9.92
E	0.0435	0.0713	6.98	18.6	12.87
G	0.0713	0.1129	10.24	18.6	8.68

Table 2 Icing tunnel test conditions [16]

Parameter	Cases		
	22A	67A	67B
V_∞, m/s	44.7	89.4	89.4
T_{tot}, °C	−7.6	−21.6	−21.6
LWC, g · m⁻³	0.78	0.55	0.55
MVD, μm	20	20	20
α	0°	0°	0°

Table 3 Heater elements materials [16]

Material	Conductivity, W · m⁻¹ · K⁻¹	Thickness, mm
Heater, alloy 90	41.0	0.03
Erosion shield, SS 301 HH	16.3	0.20
Elastomer, COX 4300	0.3	0.26
Fiber glass/epoxy composite	0.3	0.89
Silicone foam insulation	0.1	3.43

IV. Simulation Results

The reference cases were simulated with external solver ONERA2D to obtain the pressure coefficient and local efficiency collection distributions (Fig. 4). The ONERA2D results for case 67B are the same as case 67A because the flight and atmospheric

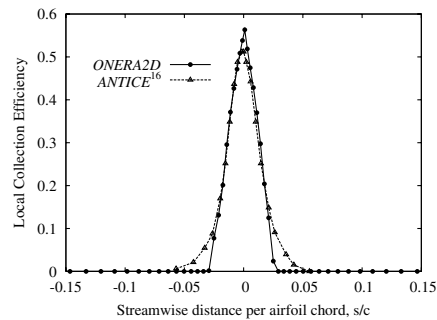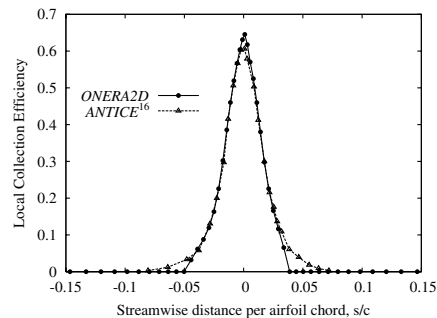**Table 4 Laminar-turbulent transition region parameters**

	Present work		Al-Khalil et al. [16]
Case	s_m/c	σ/c	s_{tr}/c
22A	0.083	0.041	0.056
67A	0.136	0.042	0.056
67B	0.048	0.020	0.035

conditions are the same. The β values estimated by ONERA2D and ANTICE are compared in Figs. 4b and 4d. There is a slight deviation among predicted values of those two codes at the impingement limit region that may be attributed to a difference in the evaluation of β.

Table 4 presents the transition parameters adopted in the present simulation to minimize the deviation between predicted and experimental values of overall heat transfer coefficients and airfoil solid surface temperatures. The region, where the transition from laminar to turbulent flow regimes occurs, is statistically described [1,17] by a mean position s_m/c and standard deviation σ/c. Al-Khalil et al. [16] adopted as abrupt transition point locations s_{tr}/c for wet and dry regimes (see Table 4), however, the procedure used to estimate the heat transfer coefficient in the transition region was not disclosed. Apropos, all the transition position locations adopted by Al-Khalil et al. [16] are within the transition region defined in the present work, which is assumed to start at position $s_m - 2 \cdot \sigma$ and end at $s_m + 2 \cdot \sigma$. The laminar to turbulent flow transition model as well as the heat transfer coefficient and friction coefficient calculation procedures are described in part 1 of this set of papers [1].

For case 22A (Fig. 5a), the overall heat transfer coefficient predicted by the present code shows agreement with experimental data within an experimental error margin in an all-protected area. In addition, an acceptable deviation is verified for case 67A (Fig. 6a) and 67B (Fig. 7a), however, some deviation between calculated and measured U values is observed from impingement limits to the end of water film. Basically, those deviations may be explained by the influence of liquid water rivulets in the heat transfer mechanism at wetted regions downstream the impingement limits. The definition of U is presented in part 1 of this set of papers [1].

Runback water distribution and water impingement flux estimated by the present code for cases 22A, 67A, and 67B are compared with ANTICE results in Figs. 5b, 6b, and 7b. In general, there is an acceptable agreement between predicted values by the present code
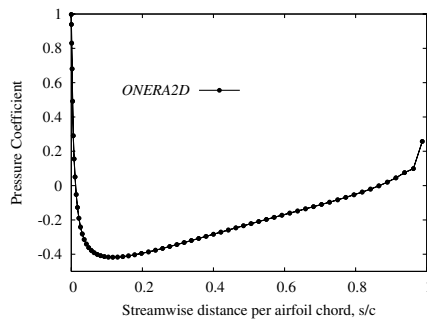
a) **Pressure coefficient, case 22A**
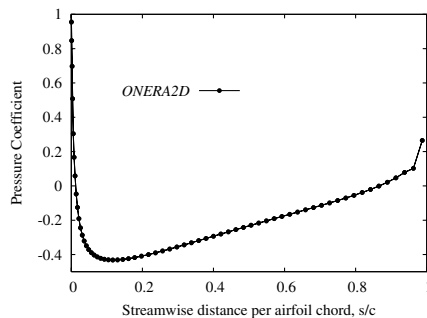
b) **Local efficiency collection, case 22A**

c) **Pressure coefficient, case 67A**

d) **Local efficiency collection, case 67A**

Fig. 4 External solver input data to present code.

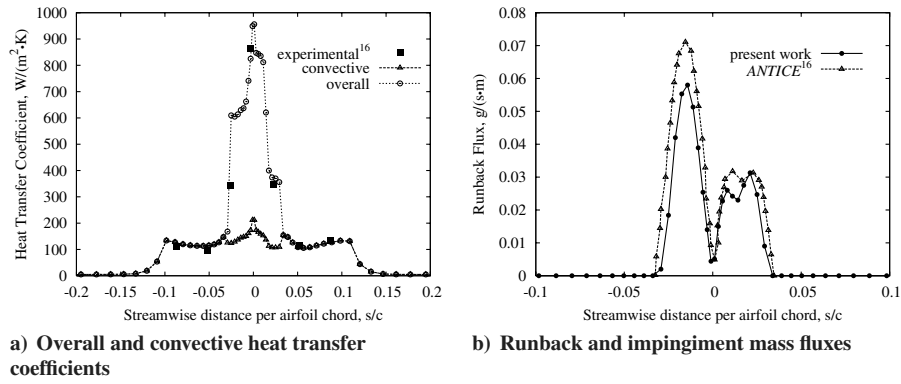a) Overall and convective heat transfer coefficients

b) Runback and impingiment mass fluxes

Fig. 5 Present work results for case 22A.

a) Overall and convective heat transfer coefficients

b) Runback and impingiment mass fluxes

Fig. 6 Present work results for case 67A.

a) Overall and convective heat transfer coefficients

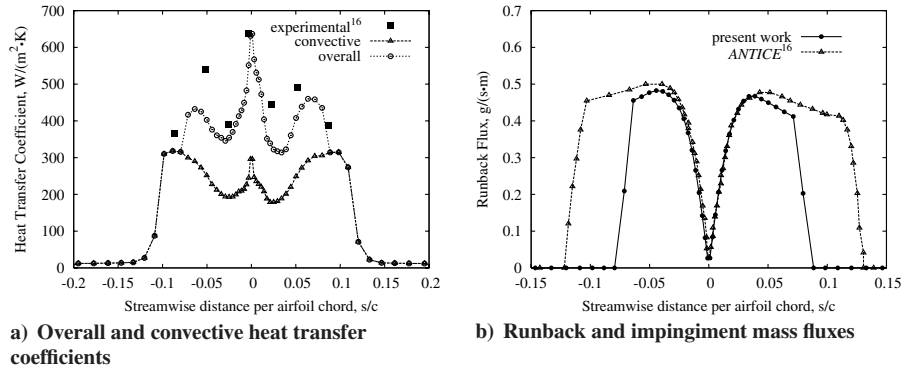b) Runback and impingiment mass fluxes
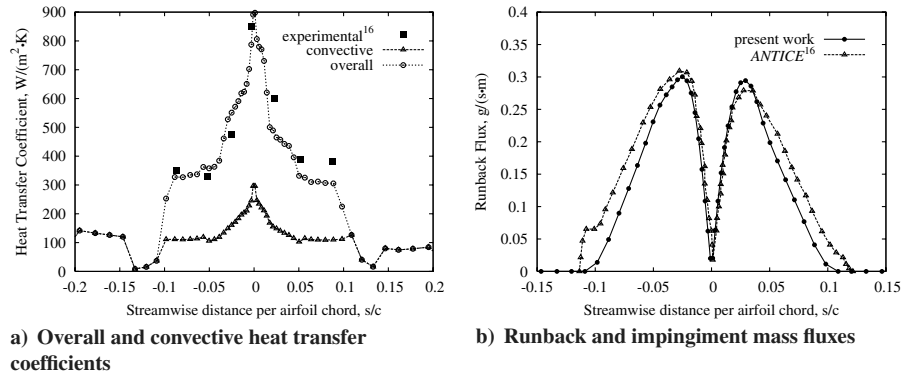
Fig. 7 Present work results for case 67B.

and ANTICE. Likely, the discrepancies observed in $\dot{m}_{run}$ may be related to different solid surface temperatures or the end of the water film position.

The solid surface temperature distribution for case 22A is shown in Fig. 8 together with the Al-Khalil et al. [16] numerical and experimental results. As shown in Figs. 5b and 8, the present code estimated that the water film will disappear at position $s/c \approx \pm 0.03$. In Fig. 8, there is a remarkable increase in measured and calculated airfoil surface temperatures when the runback water disappears. At this position, the heat transfer intensification generated by evaporative cooling ceases to occur. Consequently, a significant decrease in the overall heat transfer coefficient is observed in Fig. 5b at the end of the liquid water film. The solid surface temperature variation (dT_{wall}/ds) in the transition from wet to dry regions drives the numerical convergence and determines run time duration. To represent adequately the drying process at last wetted finite volume, without requiring a very small mesh size, a wetness factor was defined in the streamwise direction [1].

For the fully dry airfoil surfaces in case 22A, the deviations between present code results and test data are higher than wet

surfaces, however, the deviations are considered satisfactory when taking into account the two primary sources of uncertainties [18]: 1) the errors from sensors and acquisition system, and 2) the positioning errors and assembly procedures of the thermocouples and heat flux sensors on the test body. The second source of uncertainty affects the evaluation of deviation between numerical results and experimental data at locations with strong streamwise solid surface temperature gradients (dT_{wall}/ds) such as the end of the liquid water film.

Figure 9 shows the comparison between the present code predictions, Al-Khalil et al. [16] experimental data, and CANICE A and CANICE B numerical results [19] for the airfoil solid surface temperatures of case 22A. In Fig. 10, the same predictions and experimental data are compared with CANICE FD numerical results [20]. Near the end of the water film, there is an abrupt increase followed by an even sharper decrease in solid wall temperatures predicted by CANICE B (Fig. 9), however, the other two codes from same authors, CANICE A (Fig. 9) and CANICE FD (Fig. 10), do not present such a sharp variation because they use distinct convective heat transfer coefficients. There is a marked difference in how the
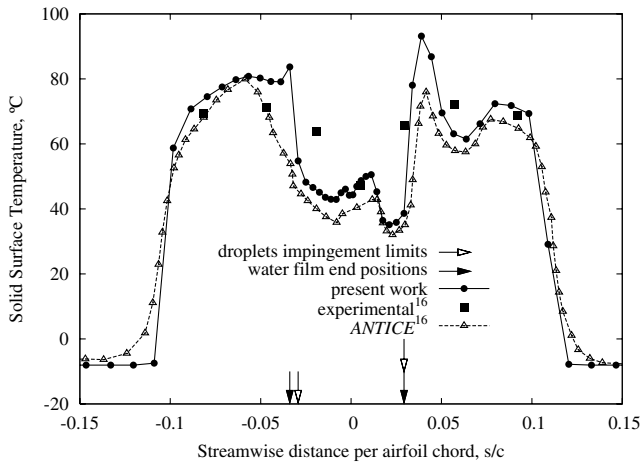
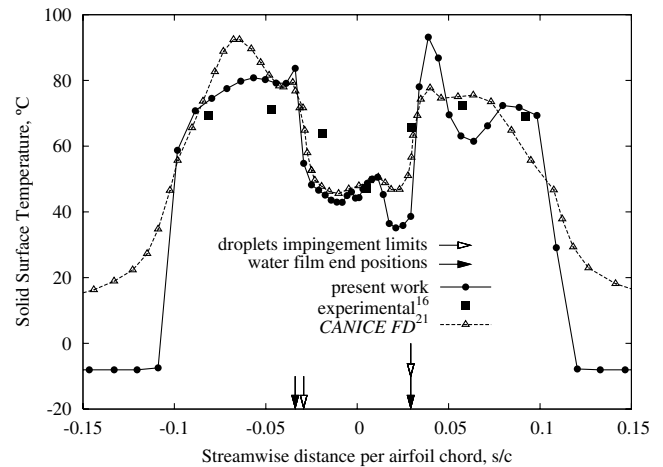**Fig. 8 Temperature distributions for case 22A: comparison with ANTICE.**

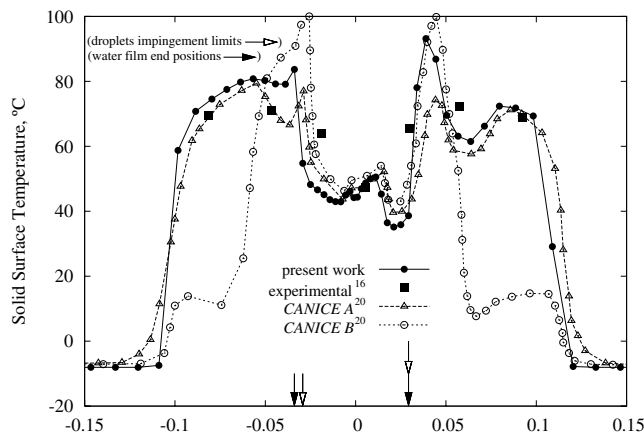**Fig. 10 Temperature distributions for case 22A: comparison with CANICE FD.**

Fig. 9 Temperature distributions for case 22A: comparison with CANICE A/B.
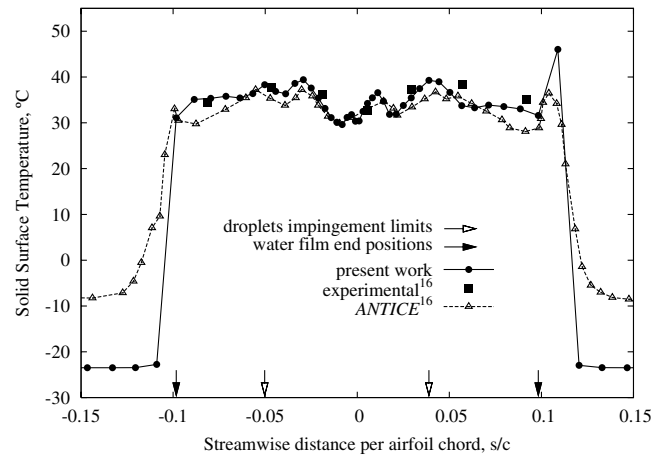

Fig. 11 Temperature distributions for case 67A: comparison with ANTICE.

codes treat the laminar to turbulent transition and define the initial conditions for turbulent thermal boundary layer evaluation. CANICE A used the experimental overall heat transfer coefficient but CANICE B solved the boundary layer equations in integral form assuming an abrupt transition. In this case, it is not clear how the virtual origin of the turbulent boundary layers was estimated when using Ambrok [21] thermal boundary layer integral analysis in CANICE B. Finally, CANICE FD [20] evaluated the boundary layer by a finite difference scheme and used the Cebeci–Smith turbulence model [22], which represents the laminar-turbulent transition with an intermittency function and an adequate continuity condition between laminar and turbulent boundary layers [23].

In case 67A, as indicated in Figs. 6b and 11, the present code estimates the water film ends at about position $s/c \approx 0.1$ at upper airfoil surface and $s/c \approx -0.1$ at lower airfoil surface due to evaporation. On the other hand, Fig. 7b shows that in case 67B the present code predicts the runback water ice formation at $s/c \approx 0.08$ and $s/c \approx -0.07$. The initial freezing rate in both upper and lower surfaces was approximately 0.4 g/(s · m).

Figure 11 shows the present model predictions, the experimental data, and the numerical results of ANTICE [16] solid surface temperature distribution for case 67A. The same predictions, experimental data, and CANICE A results [19] are presented in Fig. 12. In this case, the predictions are within the expected experimental error margin with exception of one point near position $s/c \approx 0.05$ at upper surface. As the present code does not estimate the surface wetness factor, its predicted temperatures are expected to be lower than experimental data due to the effects of water film breakdown into rivulets downstream the impingement point.

For nonprotected regions of case 22A, Fig. 9 indicates that the present code predicted surface temperatures with a trend similar to ANTICE, CANICE A and B. Nevertheless, as presented in Fig. 10, CANICE FD predicted higher temperatures than present code. Morency et al. [20] suggested that the finite difference code took into account the effect of boundary layer heating history, which may decrease the heat transfer to gaseous flow. Regarding case 67A (Figs. 11 and 12), the present code predicted surface temperatures at a nonprotected region close to CANICE A results but significantly apart from ANTICE. However, it is not clear which code is predicting more realistic airfoil surface temperatures because there are no experimental data in this region.

The running wet case 67B solid airfoil surface temperature distribution is presented in Fig. 13. For regions with temperatures near the freezing temperature (0°C), the present code predictions and ANTICE results are different because the thermal balance equation, applied to water runback flow, does not take into account the solidification enthalpy release effect nor the increase of dry area caused by the rivulets formation. However, case 67B is a very severe operational condition with low electrical power density. It may not be realistic for an aeronautical airfoil anti-ice system operation, which is usually designed to maintain temperatures within the airfoil protected area above that of the case 67B mean temperature level ($\approx 5°C$).

V. Conclusions

The thermal anti-ice system mathematical model was implemented and the numerical results were considered satisfactory
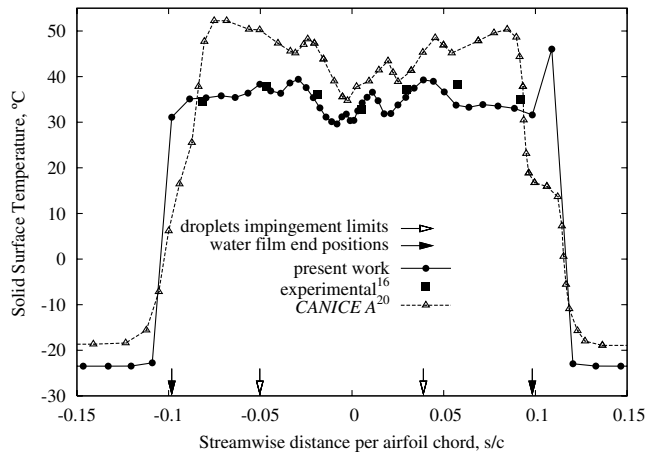
Fig. 12 Temperature distributions for case 67A: comparison with CANICE A.
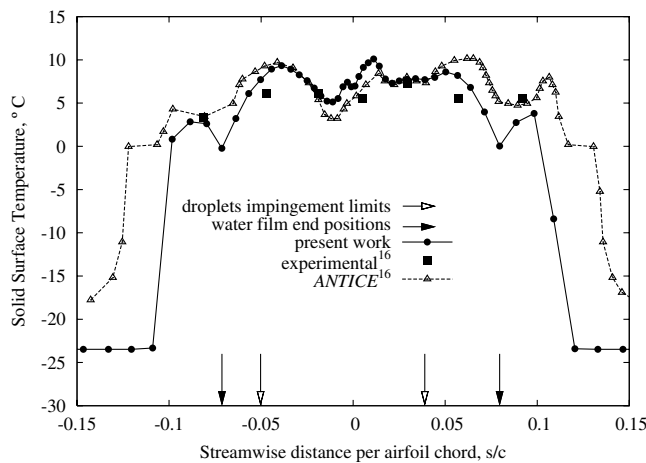

Fig. 13 Temperature distributions for case 67B: comparison with ANTICE.

for engineering purposes. From flowfield and water droplet collection efficiency results, provided by an external solver, the present numerical code is able to predict the main operational parameters of an airfoil electrothermal anti-ice system (solid surface temperature, runback water, and convection heat transfer coefficient distributions) at reference cases conditions with acceptable deviations from experimental results.

For most wet region extensions, the airfoil solid surface temperatures predicted by the present code were within experimental data error margin. The highest deviations from present code predictions to experimental data were found downstream impingement limits, where the solid surface temperatures were near freezing (0°C) or at the end of the liquid water film. To complicate the present analysis, all those regions with high deviation were located within the predicted laminar-turbulent transition region. For cases 22A and 67A, the present code had lower deviation from experimental data than ANTICE and even lower deviation when compared with CANICE. However, the present code had higher deviation than ANTICE in evaluation of case 67B. Likewise, the more accurate predictions of the ANTICE code downstream impingement limits for case 67B may be due to its rivulets model which is not incorporated in the present code.

The runback water numerical results of the present code have an acceptable and reasonable trend but lower than mass flow predicted by ANTICE. In addition, the local collection efficiency provided by ONERA2D presented deviations when compared with ANTICE, mainly at impingement limit positions at lower and upper surfaces. As expected, for all cases simulated, the present thermodynamic solver predicted the water film freezing in a position more upstream

than ANTICE code due to conservative assumptions in the freezing process.

The present code results have shown that the momentum and thermal boundary layer equations in integral form can be appropriately applied to anti-ice simulation in both evaporative and running wet regimes.

Acknowledgments

References

[1] Silva, G. A. L., Silvares, O. M., and Zerbini, E. J. G. J., "Numerical Simulation of Airfoil Thermal Anti-Ice Operation Part 1: Mathematical Modeling," *Journal of Aircraft* (submitted for publication).
[2] Silva, G. A. L., "Modelagem e Simulação da Operação de Sistema Antigelo Eletrotérmico de um Aerofólio," M.S. Thesis, Escola Politécnica da Univ. de São Paulo, São Paulo, Brazil, April 2002.
[3] Silva, G. A. L., and Silvares, O. M., "Airfoil Anti-Ice System Thermal Simulation," Escola Politécnica da Univ. de São Paulo, Technical Bulletin BT/PME/0207, São Paulo, Brazil, 2002.
[4] Silva, G. A. L., Silvares, O. M., and Zerbini, E. J. G. J., "Airfoil Anti-Ice System Modeling and Simulation," AIAA Paper 2003-0734, 2003.
[5] Silva, G. A. L., Silvares, O. M., and Zerbini, E. J. G. J., "Simulation of an Airfoil Electrothermal Anti-Ice System Operating in Running Wet Regime," AIAA Paper 2005-1374, 2005.
[6] Guffond, D., and Brunet, L., "Validation du Programme Bidimensionnel de Capitation," ONERA Technical Report RP 20/5146 SY, Châtillon Cedex, France, 1988.
[7] Wright, W., Gent, R., and Guffond, D., "DRA/NASA/ONERA Collaboration on Icing Research Part 2: Prediction of Airfoil Ice Accretion," NASA CR 202349, Cleveland, OH, May 1997.
[8] Bredif, M., "Fast Finite Element Method for Transonic Potential Flow Calculations," AIAA Paper 83-16755, 1983.
[9] Bredif, M., *Finite Element Method Calculation of Potential Flow Around Wings*, Ninth International Conference on Numerical Methods in Fluid Dynamics, Lecture Notes on Physics, Springer–Verlag, Berlin, Vol. 218, 1985, pp. 109–114, ISBN 3-540-13917.
[10] Macarthur, C., Keller, J., and Luers, J., "Mathematical Modeling of Airfoil Ice Accretion on Airfoils," AIAA Paper 82-36042, 1982.
[11] Ruff, G. A., and Berkowitz, B. M., "User Manual for the NASA Lewis Ice Accretion Prediction Code (LEWICE)," NASA CR-185129, 1990.
[12] Cansdale, J. T., and Gent, R., "Ice Accretion on Aerofoils in Two-Dimensional Compressible Flow: A Theoretical Model," Royal Aircraft Establishment TR 82128, Farnborough, UK, 1983.
[13] Gent, R., "TRAJICE2: Combined Water Droplet Trajectory and Ice Accretion Prediction Program For Aerofoils," Royal Aerospace Establishment TR 90054, Farnborough, UK, 1990.
[14] Makkonnen, L., "Heat Transfer and Icing of a Rough Cylinder," *Cold Regions Science and Technology*, Vol. 10, No. 2, Feb. 1985, pp. 105–116.
[15] Messinger, B. L., "Equilibrium Temperature of an Unheated Icing Surface as a Function of Air Speed," *Journal of the Aeronautical Sciences*, Vol. 20, No. 1, 1953, pp. 29–42.
[16] Al-Khalil, K. M., Horvath, C., Miller, D. R., and Wright, W., "Validation of NASA Thermal Ice Protection Computer Codes Part 3: Validation of ANTICE," NASA TM 2001-210907, Cleveland, OH, May 2001.
[17] Reynolds, W. C., Kays, W. M., and Kline, S. J., "Heat Transfer in the Turbulent Incompressible Boundary Layer 4: Effect of Location of Transtion and Prediction of Heat Transfer in a Known Transition Region," NASA Memo 12-4-58W, Washington, DC, Dec. 1958.
[18] Miller, D., Bond, T., Sheldon, D., Wright, W., Langhals, T., Al-Khalil, K., and Broughton, H., "Validation of NASA Thermal Ice Protection Computer Codes Part 1: Program Overview," NASA TM 107397, Cleveland, OH, Dec. 1996.
[19] Morency, F., Tezok, F., and Paraschivoiu, I., "Heat and Mass Transfer in the Case of an Anti-Icing System Modelization," AIAA Paper 99-0623, 1999.
[20] Morency, F., Tezok, F., and Paraschivoiu, I., "Anti-Icing System

Simulation Using CANICE," *Journal of Aircraft*, Vol. 36, No. 6, 1999, pp. 999–1006.

[21] Ambrok, G. S., "Approximate Solution of Equations for the Thermal Boundary Layer with Variations in Boundary Layer Structure," *Soviet Physics Technical Physics*, Vol. 2, No. 9, 1957, pp. 1979–1986.

[22] Cebeci, T., and Bradshaw, P., *Physical and Computational Aspects of Convective Heat Transfer*, Springer–Verlag, Berlin, 1984.

[23] Chen, K. K., and Thyson, N. A., "Extension of Emmon'S Spot Theory to Flows on Blunt Bodies," *AIAA Journal*, Vol. 9, No. 5, 1971, pp. 821–825.